Available online at www.sciencedirect.com
ScienceDirect
Composites Science and Technology 68 (2008) 1363–1375
COMPOSITES SCIENCE AND TECHNOLOGY
www.elsevier.com/locate/compscitech

Nacre: An orthotropic and bimodular elastic material

K. Bertoldi [a], D. Bigoni [b,*], W.J. Drugan [b,c]

[a] Department of Mechanical Engineering, Massachusetts Institute of Technology, Cambridge, MA, USA
[b] Dipartimento di Ingegneria Meccanica e Strutturale, Università di Trento, Via Mesiano 77, I-38050 Trento, Italy
[c] Department of Engineering Physics, University of Wisconsin-Madison, WI, 53706, USA

Received 30 August 2007; received in revised form 14 November 2007; accepted 29 November 2007
Available online 14 December 2007

Abstract

A new micromechanical model for nacre (mother-of-pearl) is proposed, based on an accurate description of the actual microstructure of the material. In the small-strain regime (where damage and fracture are excluded), it is shown via homogenization techniques that the mechanical behaviour of nacre is: (i) orthotropic, with a strong difference in directional stiffnesses; (ii) bimodular (different Young's moduli in tension and compression). A simple closed-form analytical solution, and a highly-accurate boundary-elements-based numerical analysis, are developed to evaluate the macroscopic behaviour of nacre from the mechanical properties of its constituents. It is shown that the predictions of our simple analytical model are in excellent agreement with the highly-accurate numerical analysis and with existing experimental data, and it is explained how our model can be further verified through new experiments. Importantly, we show that it is essential to account for nacre's bimodularity and anisotropy for the correct interpretation of published (and future) experimental data.

Keywords: Mother-of-pearl; Biological composites; Masonry; Homogenization theory; Elasticity

1. Introduction

The surprisingly excellent stiffness and toughness properties of nacre [mother-of-pearl, the internal layer of many mollusc shells (see for example Fig. 1) comprised of 95% aragonite, a mineral form of $CaCO_3$, with only a few percent of biological macromolecules] have been known since the experimental work of Currey [7,8]. The fact that these mechanical characteristics remain unchallenged by the current ceramic materials has further stimulated research. Nacre has a peculiar 'brick-mortar' microstructure (the so-called 'stretcher bond' in masonry nomenclature, see Figs. 2 and 3 and compare to Fig. 4), where stiff and flat aragonite crystals, the 'bricks' (0.2–0.9 μm thick and with a mean transversal dimension ranging between 5 and 8 μm), are connected and separated by nanoscale organic interlayers (20–30 nm, see Table 1), the 'mortar' [23,24]. While this microstructure may at least partially explain nacre's high fracture toughness, it does not seem compatible with its high stiffness. The high fracture toughness could be related to crack blunting/branching, as suggested by Almqvist et al. [1], where it is, however, concluded that ceramics with a microstructure mimicking mother-of-pearl, though superior to other ceramics, do not attain the fracture toughness of nacre. Damage and fracture mechanisms in nacre are, however, not completely understood. For instance, inelastic deformations have been considered by Wang et al. [26], whereas Sarikaya et al. [22] advocate several micromechanisms to explain the outstanding strength of nacre: (a) crack blunting/branching, (b) micro-crack formation, (c) plate pullout, (d) crack bridging (ligament formation) and (e) sliding of layers. On the other hand, from available experimental data (reported in Table 1), it is difficult to understand how a composite with a highly compliant organic matrix may exhibit such a high stiffness. Therefore, Schaffer et al. [23] and Song et al. [24] advocate the presence of mineral bridges, joining the aragonite platelets through the organic matrix. However, the existence of

* Corresponding author. Tel.: +39 0461 882507; fax: +39 0461 882599.
E-mail addresses: bertoldk@mit.edu (K. Bertoldi), bigoni@ing.unitn.it (D. Bigoni), drugan@engr.wisc.edu (W.J. Drugan).

0266-3538/$ - see front matter © 2007 Elsevier Ltd. All rights reserved.
doi:10.1016/j.compscitech.2007.11.016

Fig. 1. South African Abalone shell (*Haliotis midae*, purchased in dry condition at 'Orientimport', Torrepedrera, Italy; photos taken with a Nikon D200 digital camera at the University of Trento). Left: inner part; right: outer part.

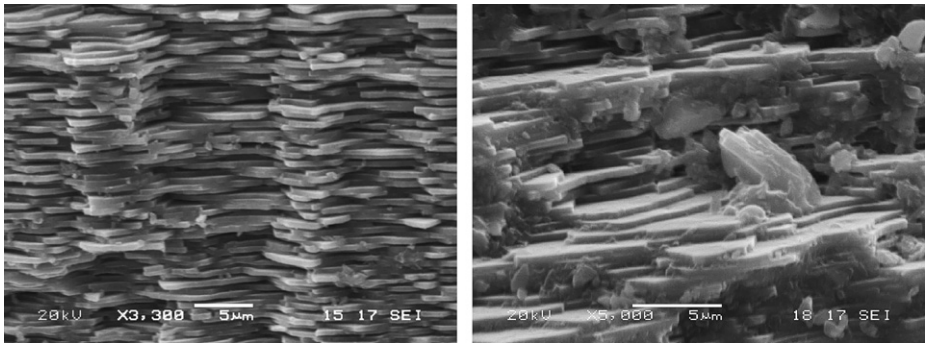

Fig. 2. A rough fracture surface of the South African Abalone shell shown in Fig. 1 [micrographs taken with a Jeol 5500 scanning electron microscope (JEOL Inc., Peabody, Mass) at the University of Trento].

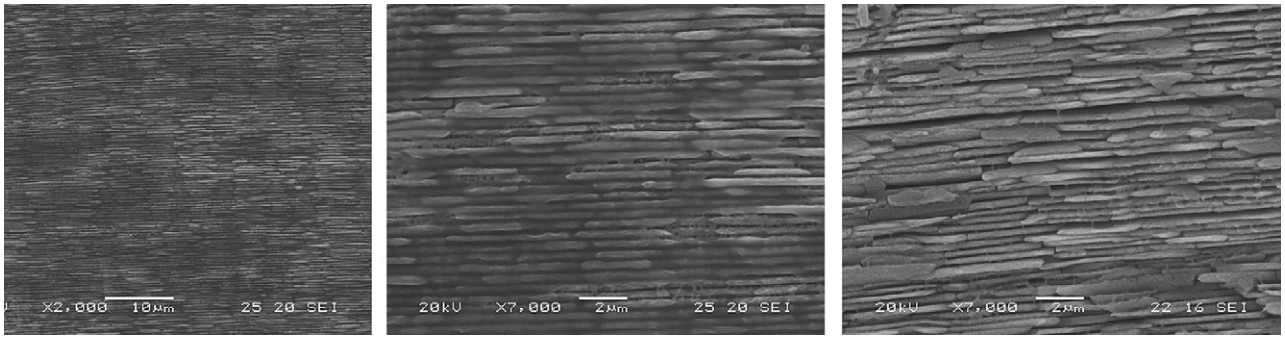

Fig. 3. A rough fracture surface of the South African Abalone shell shown in Fig. 1, etched by immersion in a 60% solution of HNO_3 for 1 h. Center and right: two details of the figure on the left, showing the 'brick-mortar' structure of nacre. Note that separations where bricks abut are evident [micrographs taken with a Jeol 5500 scanning electron microscope (JEOL Inc., Peabody, Mass) at the University of Trento].

such mineral bridges has been disproved or at least not confirmed by Bruet et al. [3] and Lin and Meyers [16].

Prior to the present work, mechanical models were incapable of explaining the high stiffness of nacre and, additionally, the anisotropy of the material (which appears evident from consideration of the microstructure) has apparently not been modeled. Nukala and Simunovic [18] employ a discrete lattice where the aragonite platelets are rigid, and use the shear-transmission hypothesis for the organic matrix. The latter hypothesis has been advocated by Ji and Gao [12], through the so-called 'tension–shear chain model', originally proposed by Jäger and Fratzl [11]. This is a simple model in which the organic matrix is assumed on the one hand not to resist tension, but to resist shear on the other. We will derive an improved version of this model and employ it for tensile response parallel to the aragonite lamellae, for which we will show it to be quite accurate. Ji and Gao [12] also note that the microstructure of nacre should imply anisotropic overall behaviour, but they do not model it. Katti et al. [14,15] measure and predict (with a finite element method) a stiffness of 20 GPa for the organic matrix and conclude that the min-

Fig. 4. An example of Roman masonry (Anfiteatro Flavio, built in the second half of the first century A.D. under Emperor Vespasiano at Pozzuoli, Naples. Photo by D. Bigoni). A detail is shown at right of the masonry in the upper left part of the figure at left.

Table 1
Available experimental data: Young's moduli parallel and orthogonal to the lamellae, E_1 and E_2, of the aragonite platelets, E_p, and of the organic matrix, E_o; thickness of the organic layer, h_o

Authors	Material	E_1 (GPa)	E_2 (GPa)	E_p (GPa)	E_o (GPa)	h_o (nm)
Jackson et al. [10]	Pinctada nacre	73	70	100	4	–
Katti et al. [14]	Red abalone	–	–	99.5	20	30
Wang et al. [26]	Abalone	69 ± 7	66 ± 2	–	–	20
	Pearl oyster	77 ± 12	81 ± 4	–	–	20
Bruet et al. [3]	Trochus niloticus	–	–	92–79	–	30-300
Barthelat et al. [4]	Red abalone	–	–	79 ± 15	2.84 ± 0.27	20-40

eral bridges have no effect on the nacre averaged stiffness. Moreover, the fact that the material should be bimodular (namely, to have a Young's modulus lower in tension than in compression) has passed completely unnoticed (although this behaviour should be inferred from the Jäger and Fratzl [11] model; see, e.g., Fig. 2b of [12]) and is still awaiting quantification.

The goal of the present article is to provide a micromechanical model capable of explaining and quantifying all the above-mentioned mechanical features. Employing the detailed description of Lin and Meyers [16] allows us to formulate a micromechanical model, which through standard homogenization techniques yields the macroscopic mechanical behaviour of nacre.[1] This turns out to be:

- orthotropic, with a strong difference between normal stiffnesses and shear stiffness; in particular, nacre is much less stiff under shear than under uniaxial tension (in the two directions parallel and perpendicular to the aragonite platelets);
- bimodular, i.e. having a Young's modulus in tension smaller than in compression, in the direction parallel to the lamellae long boundaries.

These results are obtained by developing a two-dimensional, plane strain, micromechanical model of nacre (Fig. 5), yielding averaged properties through a simple analytical approach and a standard numerical procedure (based on a boundary element technique developed by us). The simple approach yields closed-form solutions to directly determine the four parameters defining the averaged properties of nacre from knowledge of the mechanical properties of the micro-constituents. The predictions of the simple approach are found to be in excellent agreement with the numerical results obtained from a much more refined model. We note finally that although our model is based on hypotheses obtained from the very recent paper by Lin and Meyers [16], our strategy of solution can be easily modified to account for new features, should these be found in the future.

Predictions of our model are shown to agree with existing experimental data, and simple formulae are provided to extract two of the four parameters defining our model from three (or four) point macroscopic bending experiments (without knowledge of the micromechanical properties). Importantly, we show that it is essential to account for nacre's bimodularity and anisotropy for correct interpretation of the experimental data.

2. Mechanical model for nacre

Our model is built on the very accurate and recent observations and data reported by Lin and Meyers [16] and is sketched in Fig. 5. In particular, the aragonite platelets are idealized as rectangular elastic isotropic blocks (with Lamé moduli λ_p and μ_p) joined along the lamellar 'long' boundaries by the organic matrix, also taken to be linearly elastic and isotropic (with Lamé moduli λ_o and μ_o). This system is deformed under plane strain conditions. It is important to note that, along the short edges of the aragonite platelets (where these abut), Lin and Meyers [16] find a simple contact without any organic

[1] We consider in this paper mechanical behaviour at small strains, so that damage leading to final failure will not be investigated here.

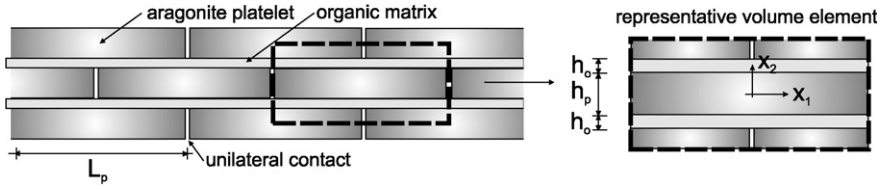

Fig. 5. Sketch of the model for the mechanical behaviour of nacre, where aragonite platelets are modeled as 'bricks' glued by a 'mortar' of organic matrix along the basal planes, but in unbonded unilateral contact along lateral surfaces.

glue. We have idealized this as a unilateral contact (so that, along the short edges, the platelets behave as perfectly jointed in compression, whereas these are completely disconnected under tension). This idealization is supported by: (i) direct observations by Lin and Meyers [16]; (ii) the fact that fracture surfaces do not cross aragonite platelets, which are seen simply to slide one with respect to the other [21,9]; (iii) the fact that the compressive strength was found to be 1.5 times the tensile strength by Menig et al. [17]; (iv) the fact that strains much larger at the tensile than at the compressive surface have been found in three-point bending by Wang et al. [26]. Clearly, the unilaterality of contact introduces a nonlinearity in the model. We will see that this can be easily handled at the cost of some approximations.

2.1. Homogenization

The above-introduced model of nacre is periodic and is very similar to typical models for masonry [19,2,5]. The goal of homogenization theory (which has been thoroughly developed for periodic elastic media, see for instance Sanchez-Palencia [20]) is to derive from a microstructure a macroscopic response valid for an effective continuous equivalent medium. To this purpose, a representative volume element is considered, which, due to the symmetry of our structure, is selected as sketched in the detail of Fig. 5. The homogenization is performed in the following steps.

- The representative volume element (of volume V and external surface S having outward unit normal vector n_i) is to be subjected to prescribed mean strain $\bar{\epsilon}_{ij}$. To this purpose, the average strain theorem (e.g., [13])
$$\bar{\epsilon}_{ij} = \frac{1}{V}\int_V \epsilon_{ij}\,\mathrm{d}V = \frac{1}{2V}\int_S (u_i n_j + u_j n_i)\,\mathrm{d}S, \tag{1}$$
(where u_i is the displacement vector, ϵ_{ij} the related strain) allows us to prescribe the mean strain in terms of an appropriate displacement on the boundary.
- The mean stress $\bar{\sigma}_{ij}$ produced by the application of the mean strain must be (numerically or analytically) evaluated on the representative volume element. The average stress theorem (e.g., [13])
$$\bar{\sigma}_{ij} = \frac{1}{V}\int_V \sigma_{ij}\,\mathrm{d}V = \frac{1}{V}\int_S \sigma_{ik} n_k x_j\,\mathrm{d}S, \tag{2}$$
(where x_j is the position vector and σ_{ij} the stress tensor) allows us to work in terms of tractions on the boundary.
- With the two steps above, an average strain/average stress relation is found, which, when compared to a effective stress/strain relation of the type
$$\bar{\sigma}_{ij} = \overline{\mathbb{E}}_{ijhk}\bar{\epsilon}_{hk}, \quad \bar{\epsilon}_{ij} = \overline{\mathbb{E}}^{-1}_{ijhk}\bar{\sigma}_{hk}, \tag{3}$$
yields the determination of all independent material constants defining the composite modulus tensor $\overline{\mathbb{E}}_{ijhk}$.

Due to the peculiar microstructural geometry, it is well-known that masonry loaded in-plane follows an anisotropic elastic description. Surprisingly, the fact that the microstructure of nacre (which is almost identical to masonry) implies an anisotropic elastic macroscopic response appears never to have been modelled. For the microstructure of nacre, the effective elastic tensor $\overline{\mathbb{E}}_{ijhk}$ is orthotropic, which in a two-dimensional setting has only the following non-null components

$$\overline{\mathbb{E}}_{1111} = \frac{\overline{E}_1}{1-\bar{\nu}_{12}\bar{\nu}_{21}}, \quad \overline{\mathbb{E}}_{2222} = \frac{\overline{E}_2}{1-\bar{\nu}_{12}\bar{\nu}_{21}}, \overline{\mathbb{E}}_{1122} = \frac{\overline{E}_1\bar{\nu}_{21}}{1-\bar{\nu}_{12}\bar{\nu}_{21}},$$
$$\overline{\mathbb{E}}_{2211} = \frac{\overline{E}_2\bar{\nu}_{12}}{1-\bar{\nu}_{12}\bar{\nu}_{21}}, \quad \overline{\mathbb{E}}_{1212} = \overline{\mathbb{E}}_{1221} = \overline{\mathbb{E}}_{2121} = \overline{\mathbb{E}}_{2112} = \overline{G}_{12}. \tag{4}$$

The inverse tensor $\overline{\mathbb{E}}^{-1}_{ijhk}$ has the following non-null components

$$\overline{\mathbb{E}}^{-1}_{1111} = \frac{1}{\overline{E}_1}, \quad \overline{\mathbb{E}}^{-1}_{2222} = \frac{1}{\overline{E}_2}, \quad \overline{\mathbb{E}}^{-1}_{1122} = -\frac{\bar{\nu}_{21}}{\overline{E}_2}, \quad \overline{\mathbb{E}}^{-1}_{2211} = -\frac{\bar{\nu}_{12}}{\overline{E}_1},$$
$$\overline{\mathbb{E}}^{-1}_{1212} = \overline{\mathbb{E}}^{-1}_{1221} = \overline{\mathbb{E}}^{-1}_{2121} = \overline{\mathbb{E}}^{-1}_{2112} = \frac{1}{4\overline{G}_{12}}, \tag{5}$$

where $\bar{\nu}_{12}$, $\bar{\nu}_{21}$ are the two plane strain Poisson ratios, and $\overline{E}_1$, $\overline{E}_2$, $\overline{G}_{12}$ are the two plane strain elastic tensile moduli and the plane strain shear modulus, subject to the symmetry condition

$$\frac{\bar{\nu}_{12}}{\overline{E}_1} = \frac{\bar{\nu}_{21}}{\overline{E}_2}, \tag{6}$$

so that through the homogenization technique we must identify *four independent material constants*. Note that in the particular case of isotropy, the four constants reduce to the two plane strain constants

$$\overline{E}_1 = \overline{E}_2 = \frac{\overline{E}}{1-\bar{\nu}^2}, \quad \bar{\nu}_{21} = \bar{\nu}_{12} = \frac{\bar{\nu}}{1-\bar{\nu}}, \tag{7}$$

in which $\overline{E}$ and $\bar{\nu}$ are the usual (three-dimensional) elastic constants (Young's modulus and Poisson's ratio).

The above four constants can be identified by subjecting the representative volume element to three independent

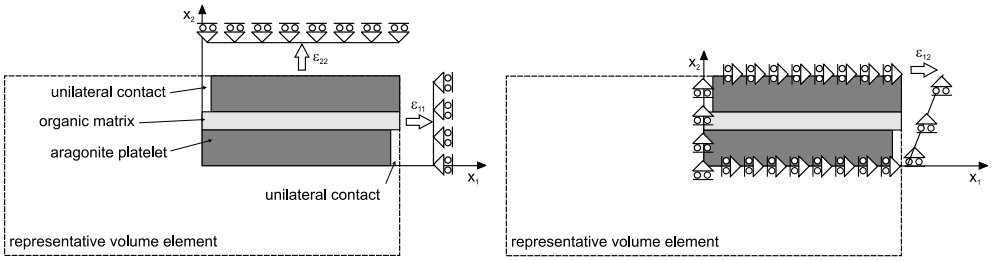

Fig. 6. The three modes of deforming the representative volume element shown in Fig. 5 needed to determine the four constants comprising the effective constitutive tensor, Eq. (4).

deformation components (which, employing the symmetries present, can be reduced to the three boundary displacements illustrated in Fig. 6), calculating the corresponding averaged stress components and comparing to Eq. (3).

2.2. A simple, closed-form homogenization model for nacre

To develop simple, closed-form formulae for the anisotropic and bimodular elastic response of nacre, we begin by observing that simple mechanical considerations suggest that the unilateral contact between aragonite platelets plays an important role only under tension aligned parallel to the x_1 axis. On the other hand, when subject to compression along the x_1 axis, tension/compression parallel to the x_2 axis, and shear parallel to the axes, the unilaterality of the contact plays a negligible role and the material behaves as a laminated medium composed of aragonite and organic matrix layers. The accuracy of these assumptions was confirmed by use of a more refined numerical model.

2.2.1. Unilateral model: determination of $\overline{E}_1^{\mathrm{t}}$ for tensile loadings

The response to a tensile loading parallel to the x_1 axis, where the aragonite platelets are disconnected (where these abut), can be obtained by borrowing and improving results from Jäger and Fratzl [11] (see [12], their Eq. (5)). This simple model is based on the fact that under such an applied tensile stress, the mineral plates carry most of the tensile load, while the organic matrix transfers the load between the plates via shear. The effective modulus of the composite for tensile loading along axis x_1, $\overline{E}_1^{\mathrm{t}}$, can be expressed in our notation (see Fig. 5) as [12]

$$\overline{E}_1^{\mathrm{t}} = \frac{E_{\mathrm{p}}}{\left(\frac{h_{\mathrm{o}}}{h_{\mathrm{p}}}+1\right)\left(4\frac{E_{\mathrm{p}}h_{\mathrm{p}}h_{\mathrm{o}}}{G_{\mathrm{o}}L_{\mathrm{p}}^2}+1\right)}, \tag{8}$$

where G_{o} denotes the shear modulus of the organic matrix, E_{p} the Young's modulus of the aragonite platelets, h_{p} and h_{o} the thicknesses of the aragonite platelets and of the organic layer, and L_{p} the aragonite platelets' length.

With the goal of generalizing (8) so that its improvement agrees more closely with our accurate numerical calculations, we derive it as follows. First, we consider the limiting case in which the composite material is considered to be made up of infinitely rigid (aragonite) platelets and soft (organic) layers. When pulled in tension, the material deforms as sketched in Fig. 7, left. Since the only deformation is the shearing of the soft layers, assuming uniform shearing of the soft layers[2] yields the elastic modulus as

$$\overline{E}_1^{\mathrm{t}} = \frac{(L_{\mathrm{p}}-\beta)L_{\mathrm{p}}G_{\mathrm{o}}}{4h_{\mathrm{o}}(h_{\mathrm{o}}+h_{\mathrm{p}})}. \tag{9}$$

where $L_{\mathrm{p}} \geqslant \beta \geqslant 0$ is a length parameter, accounting for the fact that the uniform shearing solution violates moment equilibrium of the shearing stresses where the soft layers are separated. Therefore, parameter β allows us to account for the fact that there is a small transition zone where σ_{12} increases from zero to its full value, so $\beta \ll L_{\mathrm{p}}$.

Second, we consider now the other limiting case, in which the soft (organic) layers are absent (Fig. 7, right) and the (aragonite) platelets are elastic and perfectly bonded to each other. Subjecting this structure to longitudinal loading and neglecting deformation of the layer near the detachment zones we obtain[3]

$$\overline{E}_1^{\mathrm{t}} = \frac{E_{\mathrm{p}}}{4\frac{\alpha}{L_{\mathrm{p}}}+1}, \tag{10}$$

where the length parameter α ($L_{\mathrm{p}}/4 \geqslant \alpha \geqslant 0$) has been introduced. This is similar to the parameter β and permits us to account for the fact that there is a small transition zone, at the unbonded platelet end, in which σ_{11} increases from zero to its full value, so $\alpha \ll L_{\mathrm{p}}$. When the transition zone length is zero (i.e. $\alpha = 0$) the elastic modulus is that of the intact material. Clearly the behaviour of the actual composite lies between these limiting cases. Combining, therefore, the two limiting cases as springs in series (i.e. summing the compliances) in proportion to the volume

[2] It can be shown using the theorem of minimum potential energy that the assumption of uniform shearing yields an upper bound to $\overline{E}_1^{\mathrm{t}}$, given by Eq. (9) with $\beta = 0$.

[3] It can be shown using the theorem of minimum potential energy that the assumption of uniform longitudinal strain yields an upper bound to $\overline{E}_1^{\mathrm{t}}$, given by Eq. (10) with $\alpha = 0$.

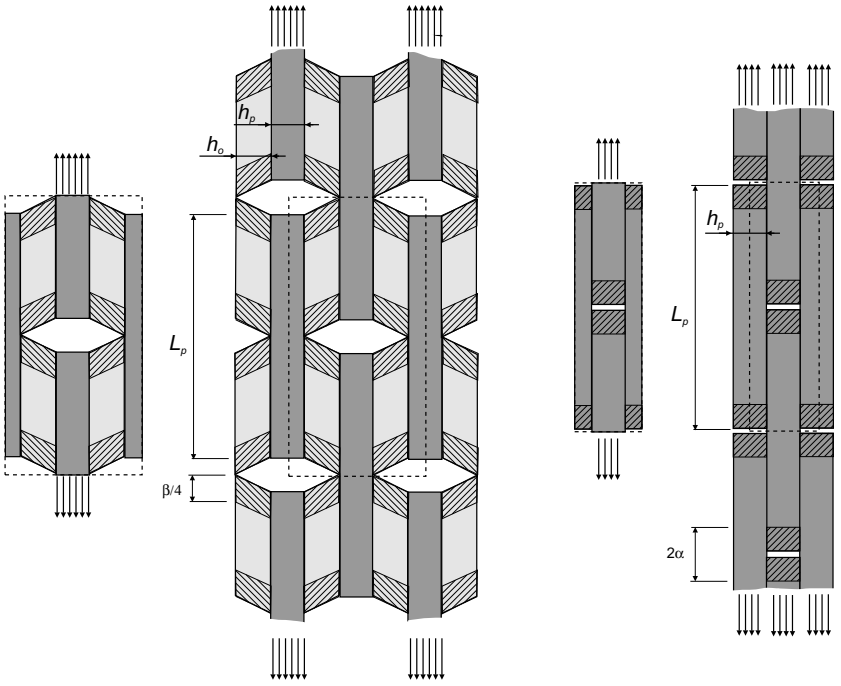

Fig. 7. The Jäger–Fratzl–Ji–Gao model in the limit cases of rigid platelets (left) and null thickness of the organic layers (right). Transition zones of lengths α and β have been introduced into the models (shown dashed).

fraction of each material, where the platelet volume fraction is

$$\Phi = \frac{h_p}{h_o + h_p}, \tag{11}$$

($\Phi = 1$ corresponds to the limiting case shown at Fig. 7 right, while $\Phi = 0$ to the limiting case shown at Fig. 7 left) we obtain

$$\frac{1}{\overline{E}_1^t} = \frac{4h_p^2(1-\Phi)}{L_p(L_p-\beta)G_o\Phi^2} + \frac{4\frac{\alpha}{L_p}+1}{\Phi E_p}. \tag{12}$$

Eq. (12) can be rewritten as

$$\overline{E}_1^t = \frac{E_p}{\left(\frac{h_o}{h_p}+1\right)\left(4\frac{E_p h_p h_o}{G_o L_p(L_p-\beta)} + \frac{4\alpha}{L_p}+1\right)}, \tag{13}$$

which is a generalization of the Jäger–Fratzl–Ji–Gao model, in the sense that this model is retrieved when $\alpha = \beta = 0$.

Since parameter β/L_p is small, we can define a new parameter γ as

$$\frac{\gamma}{L_p} = \frac{E_p h_p h_o}{G_o L_p^2}\frac{4\beta}{L_p} + \frac{4\alpha}{L_p}, \tag{14}$$

so that a Taylor series expansion of Eq. (13) in β/L_p and then use of Eq. (14) yields

$$\overline{E}_1^t = \frac{E_p}{\left(\frac{h_o}{h_p}+1\right)\left(4\frac{E_p h_p h_o}{G_o L_p^2} + \frac{\gamma}{L_p}+1\right)}, \tag{15}$$

again reducing to the Jäger–Fratzl–Ji–Gao model, when $\gamma = 0$. Eq. (15) will be shown to yield a more accurate approximation than Eq. (8).

2.2.2. Layered model: determination of $\overline{E}_1^c$, $\overline{E}_2$, $\bar{\nu}_{12}$ and $\bar{\nu}_{21}$ for compressive loadings

When loaded in compression or under shear, nacre behaves (following our simplifying assumptions) as a monolithic laminate material, composed of uniform isotropic laminae of thicknesses h_p and h_o (see Fig. 5). Homogenization of this type of material is standard and can be found for instance in Willis [27]. However, for completeness, we provide a sketch of the approach here. We assume $\bar{\epsilon}_{22} = \bar{\epsilon}_{12} = 0$ and $\epsilon_{11} = \bar{\epsilon}_{11} =$ constant in all laminae (so that compatibility is satisfied). Uniform σ_{11} and σ_{22} are generated, the former different in each lamina (but trivially satisfying equilibrium) and the latter must be required to be equal in each lamina (and equal to the mean value $\bar{\sigma}_{22}$) by equilibrium considerations at the interface. It follows that in a generic layer (having elastic constants E and ν)

$$\sigma_{11} = \frac{\bar{\epsilon}_{11}E + \bar{\sigma}_{22}\nu(1+\nu)}{1-\nu^2}. \tag{16}$$

Using Eq. (16) in the condition $\bar{\epsilon}_{22} = 0$, valid for the unit cell, we obtain

$$\overline{\mathbb{E}}_{2211} = \frac{\bar{\sigma}_{22}}{\bar{\epsilon}_{11}} = \left\langle \frac{\nu}{1-\nu} \right\rangle \left\langle \frac{(1+\nu)(1-2\nu)}{E(1-\nu)} \right\rangle^{-1}, \tag{17}$$

where the bracket $\langle\rangle$ is used to denote the mean value of a generic function ψ as follows

$$\langle \psi(E,\nu) \rangle = \frac{h_o\psi(E_o,\nu_o) + h_p\psi(E_p,\nu_p)}{h_o + h_p}. \tag{18}$$

Using Eq. (17) in Eq. (16) and averaging, we obtain

$$\overline{\mathbb{E}}_{1111} = \frac{\bar{\sigma}_{11}}{\bar{\epsilon}_{11}} = \left\langle \frac{E}{1-\nu^2} \right\rangle + \left\langle \frac{\nu}{1-\nu} \right\rangle^2 \left\langle \frac{(1+\nu)(1-2\nu)}{E(1-\nu)} \right\rangle^{-1}. \tag{19}$$

Finally, we impose a mean strain whose only non-zero component is $\bar{\epsilon}_{22}$. Analogously to the previous case, we obtain for a generic layer (defined by E and ν)

$$\sigma_{11} = \frac{\bar{\sigma}_{22}\nu}{1-\nu}, \tag{20}$$

so that

$$\overline{\mathbb{E}}_{2222} = \frac{\bar{\sigma}_{22}}{\bar{\epsilon}_{22}} = \left\langle \frac{1-\nu-2\nu^2}{E(1-\nu)} \right\rangle^{-1}. \tag{21}$$

Hence, the effective elastic constants $\overline{E}_1^c$, $\overline{E}_2$, $\bar{\nu}_{12}$ and $\bar{\nu}_{21}$ can be determined by employing Eq. (4) as

$$\begin{aligned}
\overline{E}_1^c &= \frac{E_o h_o (1-\nu_p^2) + E_p h_p (1-\nu_o^2)}{(h_o+h_p)(1-\nu_p^2)(1-\nu_o^2)},\\
\overline{E}_2 &= \frac{E_o E_p (h_o+h_p)[E_o h_o (1-\nu_p^2) + E_p h_p (1-\nu_o^2)]}{\Gamma},\\
\bar{\nu}_{21} &= \frac{E_o E_p (h_o+h_p)(1+\nu_p)(1+\nu_o)[\nu_o h_o (1-\nu_p) + \nu_p h_p (1-\nu_o)]}{\Gamma},\\
\bar{\nu}_{12} &= \frac{\nu_o h_o (1-\nu_p) + \nu_p h_p (1-\nu_o)}{(h_o+h_p)(1-\nu_p)(1-\nu_o)},
\end{aligned} \tag{22}$$

where

$$\begin{aligned}
\Gamma = {} & h_o h_p [E_p^2 (1+\nu_o)^2 (1-2\nu_o) + E_o^2 (1+\nu_p)^2 (1-2\nu_p)\\
& + 2E_o E_p \nu_o \nu_p (1+\nu_p)(1+\nu_o)]\\
& + E_o E_p (h_o^2 + h_p^2)(1-\nu_p^2)(1-\nu_o^2).
\end{aligned} \tag{23}$$

2.2.3. Layered model: determination of $\overline{G}_{12}$

In order to determine the effective shear modulus of the composite, we consider again the monolithic layered model considered before and we prescribe a mean strain $\bar{\epsilon}_{12}$, requiring $\sigma_{12} = \bar{\sigma}_{12}$ in all layers. We obtain

$$\overline{G}_{12} = \overline{\mathbb{E}}_{1212} = \frac{\bar{\sigma}_{12}}{\bar{\epsilon}_{12}} = \frac{1}{2}\left\langle \frac{1+\nu}{E} \right\rangle^{-1}, \tag{24}$$

which becomes

$$\overline{G}_{12} = \frac{E_o E_p (h_o+h_p)}{2[E_p h_o (1+\nu_o) + E_o h_p (1+\nu_p)]}. \tag{25}$$

Formulae (15), (22), and (25) represent the results of our simple homogenization approach; these allow a relation between the micromechanical geometry and properties and the macroscopic, effective behaviour. As a simple check, note that in the special case $E_o = E_p = E$ and $\nu_o = \nu_p = \nu$, Eqs. (22) and (25) yield the correct plane strain isotropic constants: $\overline{E}_1 = \overline{E}_2 = E/(1-\nu^2)$, $\bar{\nu}_{12} = \bar{\nu}_{21} = \nu/(1-\nu^2)$, and $\overline{G}_{12} = E/(2+2\nu)$.

It should be noted that in order to use the bimodular model that we propose for stress states different from uniaxial tension or compression, a criterion for dividing strain space into compression and tension subdomains is needed (something analogous to a yield criterion in strain space plasticity), and continuity of the stress/strain law should be enforced (see [6] for details). We do not pursue this subject further here.

2.3. Results from a boundary-elements-based numerical technique

Since via the averaging theorems we can work with displacements and tractions on the surface of the representative volume element, a numerical boundary element technique seems to be particularly appropriate. We have used a general-purpose Fortran 90 code for two-dimensional analysis.[4] In the code, linear (constant) shape functions for the displacements (tractions) at the boundary are assumed, and the material has been taken to be linear elastic, with Lamé moduli λ and μ. The unit cell (see Fig. 5) has been discretized along boundaries parallel to the x_1 axis employing 50 elements and along the boundaries parallel to the x_2 axis using 20 elements for the aragonite platelets and 10 elements for the organic matrix layer. Following Sarikaya et al. [22], the thickness of the aragonite plates and of the interlayers have been chosen respectively as $h_p = 0.5\ \mu m$ and $h_o = 20\ nm$, while the length of the plates has been selected as $L_p = 5\ \mu m$.

In the numerical analyses, both the aragonite plates and the organic interphase have been modelled as linear elastic materials, having Young's moduli $E_p = 100\ GPa$ and E_o ranging between 0 and 10 GPa to cover the range of values experimentally measured (see Table 1) (the Poisson ratio has been taken equal to 0.33 for both materials). The unilaterality of the contact has been accounted for by using a small gap where platelets abut and confirming that this gap opens under tensile applied loading, while no gap was used under compressive loading.

Results of the analysis are reported in Figs. 8 and 9, together with the predictions of the simple analytical formulae, Eqs. (22) and (25) and the Jäger–Fratzl–Ji–Gao model, Eq. (8), and our improved version, Eq. (15), with $\gamma = 0.26\, L_p$ and labelled 'Proposed model'. In Fig. 8 the effective moduli (normalized by E_p) are reported versus the normalized Young's modulus of the organic matrix, E_o/E_p, while the same effective moduli are reported versus the thicknesses ratio h_o/h_p (see Fig. 5) in Fig. 9. The numerical simulations reported in Figs. 8 and 9 have been performed under both the assumptions of disconnection (tensile loading) and perfect contact (compressive loading) at the unilateral contact between aragonite platelets. The results show clearly that the unilaterality of the contact only plays a significant role for tension parallel to x_1 axis

[4] This code has been developed at the Computational Solids & Structural Mechanics Laboratory of the University of Trento, whose executable is available at: http://www.ing.unitn.it/dims/laboratories/comp_solids_structures.php.

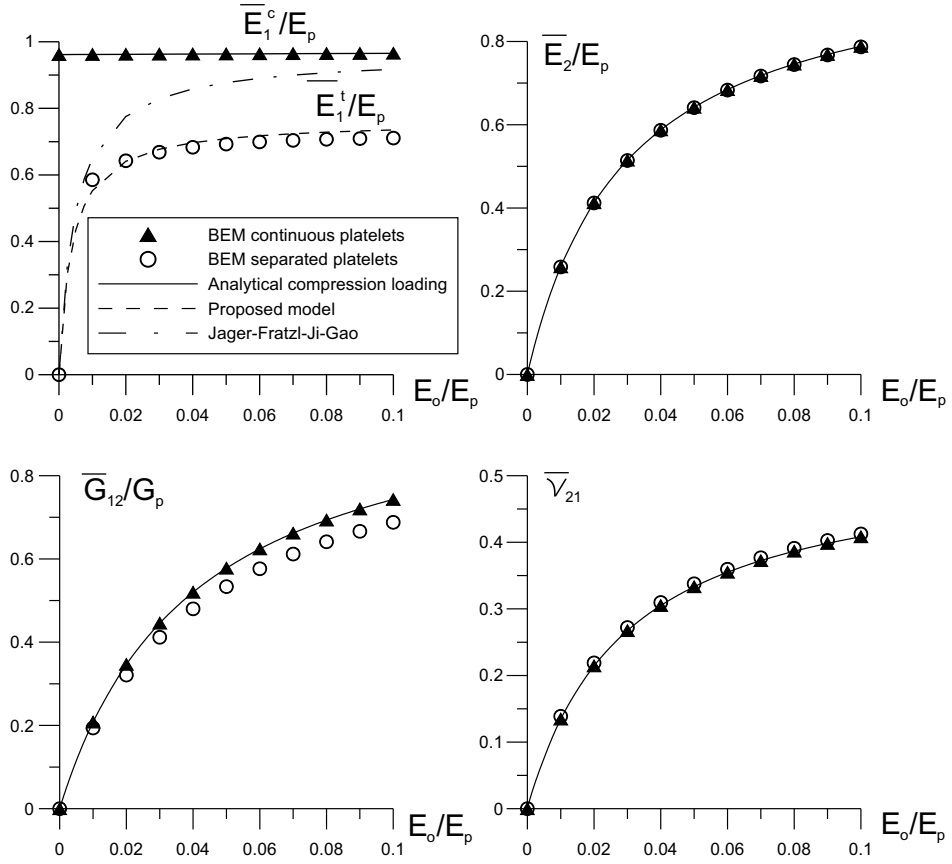

Fig. 8. Effective elastic moduli calculated numerically and from the simple formulae (8), (15) (with $\gamma = 0.26\,L_p$), (22) and (25).

(there is a small effect in the shear case). Moreover, it is clear from Figs. 8 and 9 that the agreement with the simple theory, Eqs. (15), (22) and (25), is excellent.

Note also that formula (15), employed with $\gamma = 0.26\,L_p$, clearly improves upon that of Ji and Gao [12], Eq. (8), based on the Jäger and Fratzl [11] model.

It is important at this point to quantify the degree of anisotropy and bimodularity of the material, since these two properties have not previously been modelled for nacre. To this purpose, we report in Fig. 10 the tension/compression ratio of the effective Young's moduli $\overline{E}_1^t/\overline{E}_1^c$ (equal to 1 when bimodularity is absent) and in Fig. 11 the ratios $\overline{E}_1^t/\overline{E}_{Av}$, $\overline{E}_1^c/\overline{E}_{Av}$, $\overline{E}_2/\overline{E}_{Av}$, $\overline{G}_{12}/\overline{G}_{Av}$, where

$$\overline{E}_{Av} = \frac{\overline{E}_1^t + \overline{E}_1^c + \overline{E}_2}{3}, \quad \overline{\nu}_{Av} = \frac{\overline{\nu}_{12}^t + \overline{\nu}_{12}^c + \overline{\nu}_{21}}{3},$$
$$\overline{G}_{Av} = \frac{\overline{E}_{Av}}{2(1+\overline{\nu}_{Av})}, \tag{26}$$

so that the ratios are equal to 1 in the case of isotropy and equal behaviour in tension and compression.

To better quantify the anisotropy and bimodularity effects, we introduce a (unit norm) uniaxial stress in the direction of the unit vector n_i as

$$\sigma_{ij} = \pm n_i n_j, \tag{27}$$

(taken positive for tension and negative for compression) so that the normal stress and strain components in the direction n_i are

$$\sigma_{nn} = \pm 1, \quad \epsilon_{nn} = n_i \epsilon_{ij} n_j = \pm n_i n_j \overline{\mathbb{E}}_{ijhk} n_h n_k. \tag{28}$$

Since in plane strain n_i becomes a function of the inclination angle θ with respect to the x_1 axis, we can define the elastic moduli in tension and compression, respectively, $\overline{E}^t(\theta)$ and $\overline{E}^c(\theta)$, as

$$\overline{E}^t(\theta) = \frac{1}{\overline{\epsilon}_{nn}^t(\theta)}, \quad \overline{E}^c(\theta) = -\frac{1}{\overline{\epsilon}_{nn}^c(\theta)}. \tag{29}$$

Therefore, a polar plot of Eqs. (29), obtained by using Eqs. (15), (22) and (25) in Eq. (5), allows a visual quantification of the elastic anisotropy. This is reported in Fig. 12, after normalization by $\overline{E}_1^c$. Since the graphs would reduce to unit circles in the case of isotropy and equal behaviour in tension and compression, the strong degrees of material anisotropy and bimodularity are evident.

Although parametric investigations are reported in the graphs of Figs. 10 and 11, the ratio E_o/E_p usually (see Table 1) takes values between the two cases considered in Fig. 12, namely, 0.01 and 0.04. We can, therefore, conclude that:

- the ratio $\overline{E}_1^t/\overline{E}_1^c$ ranges between 0.5 and 0.8, showing that bimodularity is an important effect (a fact previously not understood, and, therefore, not tested);

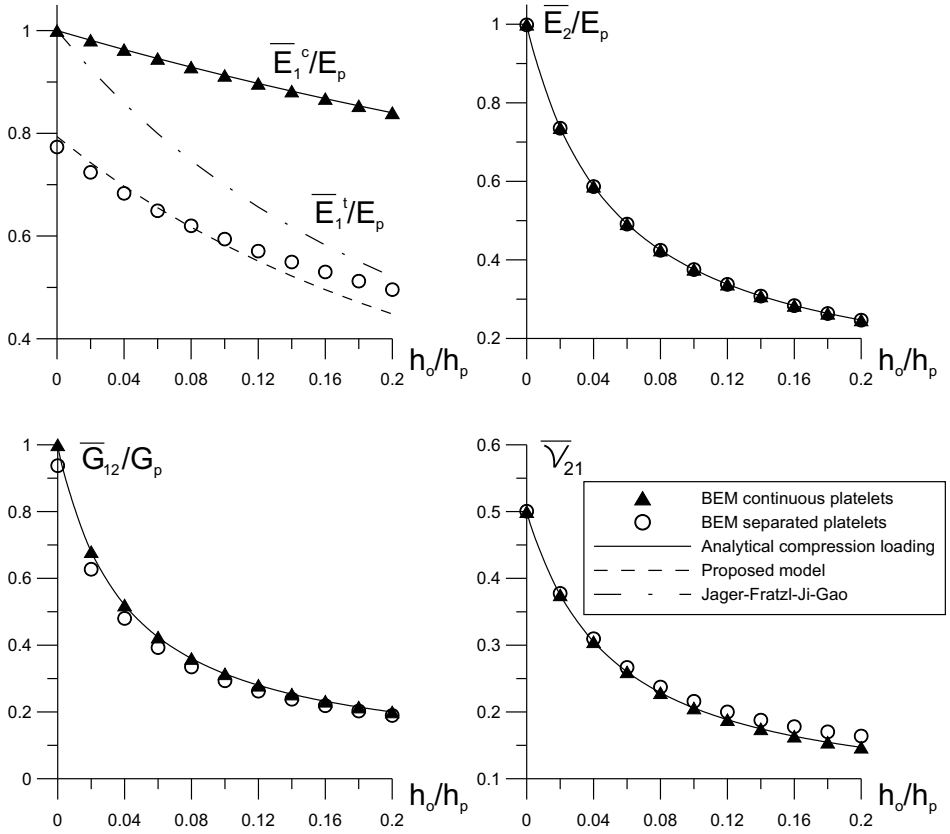

Fig. 9. Effective elastic moduli calculated numerically and from the simple formulae (8), (15) (with $\gamma = 0.26\,L_p$), (22) and (25). Modulus E_o has been taken equal to 4 GPa.

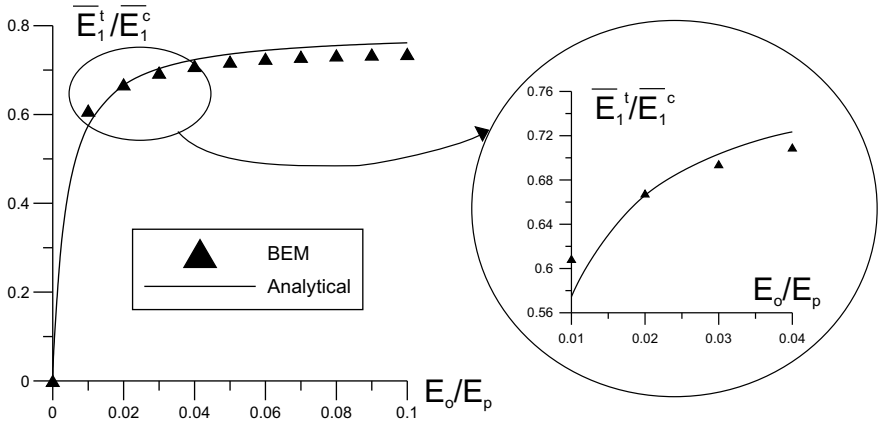

Fig. 10. Bimodularity of the material, quantified by the tension/compression ratio of the effective elastic moduli. A detail in the relevant range of parameters is given at right.

- both the ratios $\overline{E}_1^c/\overline{E}_{Av}$ and $\overline{E}_2/\overline{E}_{Av}$ lie near 1, (a fact consistent with experimental results by Jackson et al. [10] and Wang et al. [26]);
- the ratio $\overline{G}_{12}/\overline{G}_{Av}$ ranges between 0.3 and 0.6, showing a strong difference in degree of anisotropy between the shear and Young's moduli (a fact noticed also by Jackson et al. [10]).

3. Comparison with experimental data

To compare the predictions of our model with available experimental data, we refer to Table 1, where data taken from the literature are reported.

Before discussing the model's predictions, we note that the experimental results reported in Table 1 have been

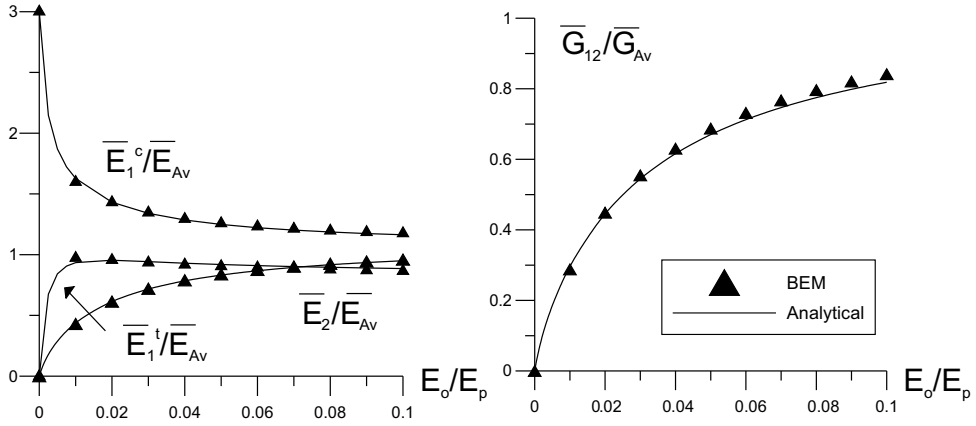

Fig. 11. Anisotropy of the material, quantified by the effective elastic moduli normalized by the directionally-averaged moduli defined in Eq. (26).

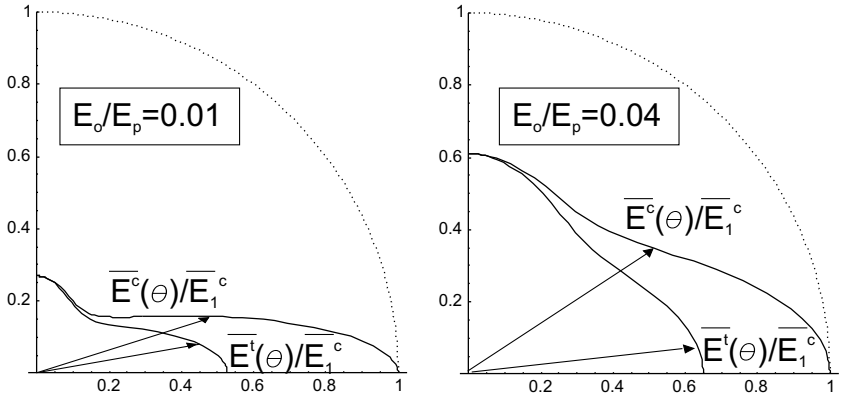

Fig. 12. Polar graphs of the effective elastic moduli in tension and compression, normalized by $\overline{E}_1^c$, revealing the strong anisotropy and bimodularity of nacre. (In the case of isotropy and in the absence of bimodularity, a single unit circle would be present in each case.)

mainly determined via three-point bending tests. These tests are usually interpreted by employing the linear theory of *unimodular isotropic* elasticity, but, in light of our findings, these should instead be interpreted with formulae valid for *bimodular, orthotropic* elasticity. These are derived in Appendix A, and summarized here:

- For three-point bending of a beam of span l, thickness h and loaded by a force per unit depth P, the deflected shape of the neutral axis is

$$u_2(x_1) = \frac{(1+\sqrt{c})^2 P x_1 (3l^2 - 4x_1^2)}{16\overline{E}_1^t h^3} + \frac{3Px_1}{5\overline{G}_{12}h}, \quad x_1 \in [0, l/2], \tag{30}$$

(where $c = \overline{E}_1^t/\overline{E}_1^c$, and $c = 1$ corresponds to equal behaviour in tension and compression) so that the mid-span vertical displacement δ divided by the applied load P is

$$\frac{\delta}{P} = \frac{(1+\sqrt{c})^2}{16\overline{E}_1^t}\left(\frac{l}{h}\right)^3 + \frac{3}{10\overline{G}_{12}}\frac{l}{h}. \tag{31}$$

- For four-point bending of a beam of span l, thickness h and loaded at $x_1 = l_0$ by a force per unit depth P (neglecting shear deformation), the deflected shape of the neutral axis is

$$u_2(x_1) = \frac{(1+\sqrt{c})^2 P x_1}{2\overline{E}_1^t h^3}(3ll_0 - 3l_0^2 - x_1^2), \quad x_1 \in [0, l_0]$$
$$u_2(x_1) = \frac{(1+\sqrt{c})^2 P l_0}{2\overline{E}_1^t h^3}(3x_1(l - x_1) - l_0^2), \quad x_1 \in [l_0, l/2] \tag{32}$$

so that the vertical displacement δ at $x_1 = l_0$, i.e. where the vertical force P is applied, is

$$\frac{\delta}{P} = \frac{(1+\sqrt{c})^2}{8\overline{E}_1^t}\frac{l_0(3l^2 - 4l_0^2)}{h^3}. \tag{33}$$

It is clear from Eqs. (31) and (33) that using three or four-point bending tests we can only identify two parameters

$$\frac{(1+\sqrt{c})^2}{\overline{E}_1^t}, \quad \text{and} \quad \overline{G}_{12},$$

so that the full exploration of bimodularity and orthotropy requires use of at least one additional test (such as for instance a direct tension or compression test or, perhaps, nanoindentation).

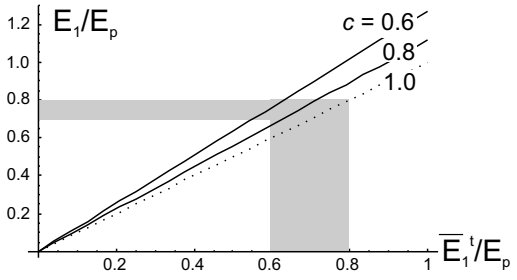

Fig. 13. Relation between the Young's moduli in the direction of the x_1 axis obtained by incorporating, and without incorporating, bimodularity, respectively $\overline{E}_1^{\mathrm{t}}$ and E_1, Eq. (34). Results are given for different values of bimodularity $c = \overline{E}_1^{\mathrm{t}}/\overline{E}_1^{\mathrm{c}}$, and the gray region indicates the parameter range of interest.

Moreover, the effect of low shear modulus $\overline{G}_{12}$ only plays a role for sufficiently high values of h/l. The experiments performed by Jackson et al. [10] refer to very low values of h/l, so that shear deformation should be negligible. However, bimodularity should play an important role in those experiments, and, therefore, the Young's modulus obtained by Jackson et al. must be corrected before comparing it to the prediction of our model. This correction can be obtained by considering Eq. (31) without shear deformation, with $c = 1$, as used by Jackson et al., and with $c < 1$, as found by us. The result is the relationship

$$E_1 = \frac{4\overline{E}_1^{\mathrm{t}}}{(1+\sqrt{c})^2}, \tag{34}$$

where E_1 is the Young's modulus in the direction of the x_1 axis, assuming equal behaviour in tension and compression. It should be noted that there is no difference between the Young's modulus in the direction of the x_2 axis found by us and by Jackson et al., since bimodularity does not play a role in that case.

Eq. (34) is plotted in Fig. 13, for the three values $c = \{1, 0.8, 0.6\}$. The grey zone denotes the parameter range of interest. We observe that the correction is significant and that we find values of E_1/E_{p} in the range 0.7–0.8, in agreement with the experimental data reported in Table 1.

4. Conclusions

Within the framework of the small-strain behaviour of nacre (mother-of-pearl), we have accounted for the first time for the facts that the material response is

- orthotropic, with low shear stiffness;
- bimodular (lower Young's modulus in tension than in compression).

To characterize this material from the knowledge of the microstructure, we have provided:

- a simple analytical model,
- and a highly-accurate numerical analysis,

both based on a sound micromechanical approach. We have also provided simple, closed-form formulae to determine two of our four macroscopic moduli directly from macroscopic three and four-point bending tests on the composite material. This provides a direct check of our constitutive model, since its macroscopic moduli are completely determined from the constituents material moduli and the composite microstructure. The comparison with available experimental data is excellent, and we expect that future experiments will further validate our model.

Acknowledgements

Financial support of MURST-Cofin 2003 (prot. 2003082105_002) (KB) and MURST-Cofin 2005 (prot. 2005085973_002) (DB) is gratefully acknowledged. WJD acknowledges support from Italian Ministry Research Grant "Rientro dei cervelli MIUR 26/1/2001".

Appendix A. Bending of an orthotropic, bimodular beam deformed in plane strain

Let us consider a bimodular beam in plane strain subjected to bending, for example, three-point bending as illustrated in Fig. 14. Since only normal strains are involved for bending, bimodularity reduces to switching between two possible behaviours as a function of the sign of the strain and stress. It is, therefore, expedient to introduce a piecewise nonlinearity for certain quantities. We denote, for instance, the elastic modulus in the direction parallel to the x_1 axis by $\widetilde{E}_1$, meaning

$$\widetilde{E}_1 = E_1^{\mathrm{t}} H(\epsilon_{11}) + E_1^{\mathrm{c}} H(-\epsilon_{11}), \tag{A.1}$$

where for conciseness bars over the symbols have been dropped, so that E_1^{t} and E_1^{c} are the two composite plane strain Young's moduli in tension and compression, respectively, and H is the Heaviside step function. An analogous use of variables with a superposed tilda will be made in the following.

For plane strain bending, it is assumed that the resultant force in the direction of the x_1 axis is null

$$\int_{-h/2}^{h/2} \epsilon_{11}(x_2)\widetilde{E}_1 \, \mathrm{d}x_2 = 0, \tag{A.2}$$

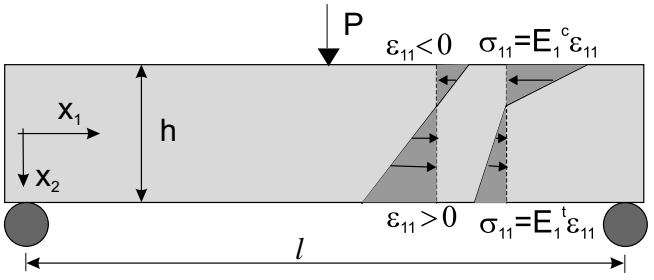

Fig. 14. Bending of a bimodular beam.

and that the applied bending moment per unit thickness M is given by

$$M = \int_{-h/2}^{h/2} \epsilon_{11}(x_2)\widetilde{E}_1 x_2 \, dx_2, \tag{A.3}$$

where h is the height of the beam. The strain component ϵ_{11} is assumed to vary linearly along the direction of the x_2 axis, so that from Eqs. (A.2) and (A.3) we obtain

$$\epsilon_{11}(x_2) = \frac{3M[h(1-c) + 2x_2(1+\sqrt{c})^2]}{2E_1^t h^3}, \tag{A.4}$$

where $c = E_1^t/E_1^c$. Therefore, the neutral axis is defined by

$$x_2 = \frac{h}{2}\frac{\sqrt{c}-1}{\sqrt{c}+1}, \tag{A.5}$$

so that its position is independent of the applied moment. From the bimodular, two-dimensional stress–strain relationship for an orthotropic material, we find

$$\epsilon_{11} = \frac{\sigma_{11}}{\widetilde{E}_1}, \quad \text{and} \quad \epsilon_{22} = -\frac{\sigma_{11}\tilde{\nu}_{12}}{\widetilde{E}_1}. \tag{A.6}$$

Integration provides the displacement field in the form

$$\begin{aligned} u_1(x_1,x_2) &= \epsilon_{11}(x_2)x_1, \\ u_2(x_1,x_2) &= -\frac{3M_z x_2[h(1-c) + x_2(1+\sqrt{c})^2]}{2E_1^t h^3}\tilde{\nu}_{12} + v_0(x_1), \end{aligned} \tag{A.7}$$

where $\epsilon_{11}(x_2)$ is given by Eq. (A.4). Since the shear strains must be zero, we find that

$$v_0(x_1) = -\frac{3(1+\sqrt{c})^2 M_z}{E_1^t h^3}\frac{x_1^2}{2} + v_1(x_1), \tag{A.8}$$

and, in order to have continuity of the displacement at the neutral axis, we get

$$v_1(x_1) = \frac{3M_z(-1+\sqrt{c})^2(\nu_{12}^t - \nu_{12}^c)}{8cE_1^c h} H(-\epsilon_{11}(x_2)). \tag{A.9}$$

The displacement components of the neutral axis are given by

$$\begin{aligned} u_1 &= 0 \\ u_2 &= \frac{3M[-4(1+\sqrt{c})^2 x_1^2 + (-1+\sqrt{c})^2 h^2 \nu_{12}^t]}{8E_1^t h^3}, \end{aligned} \tag{A.10}$$

so that the elastica is given by

$$\frac{\partial^2 u_2}{\partial x_1^2} = -\frac{3M(1+\sqrt{c})^2}{E_1^t h^3}. \tag{A.11}$$

For a simply-supported beam of span l loaded by two concentrated loads P per unit thickness (plane strain four-point bending), integration of the elastica yields (neglecting shear deformation) Eq. (32) and thus Eq. (33).

For a simply-supported beam of span l loaded by a central concentrated load P per unit thickness (plane strain three-point bending), integration of the elastica yields (neglecting shear deformation)

$$u_2(x_1) = \frac{(1+\sqrt{c})^2 P x_1(3l^2 - 4x_1^2)}{16E_1^t h^3}. \tag{A.12}$$

Since our material has a low shear modulus G_{12}, it may be important to evaluate the contribution to the elastica of shear deformability. To this purpose, we follow Jourawski's analysis (which by the way originated to take into account the high compliance of wood under shearing, [25]), thus finding for the mean shear stresses in a bimodular (plane strain) beam

$$\begin{aligned} \sigma_{12}(x_2) = \frac{3T}{8h^3 c}\{&4h^2 c - [(\sqrt{c}-1)h - 2(\sqrt{c}+1)x_2]^2 H(\epsilon_{11}(x_2)) \\ &- c(\sqrt{c}+1)(h-2x_2)[(\sqrt{c}-3)h \\ &- 2(\sqrt{c}+1)x_2]H(-\epsilon_{11}(x_2))\}, \end{aligned} \tag{A.13}$$

where T is the shear force per unit thickness.

Equating the strain energies in the beam calculated from external load and from internal stresses (or, in other words, using Clapeyron's theorem) we obtain for the shear deformability

$$\frac{\partial u_2}{\partial x_1} = \frac{6T}{5hG_{12}}, \tag{A.14}$$

so that (within the usual approximations) shear deformation is unaffected by bimodularity.

Thus, accounting for shear deformation, integration of the elastica gives Eqs. (30) and (31).

References

[1] Almqvist N, Thomson NH, Smith BL, Stucky GD, Morse DE, Hansma PK. Methods for fabricating and characterizing a new generation of biomimetic materials. Mater Sci Eng C 1999;1:37–43.

[2] Anthoine A. Derivation of the in-plane elastic characteristics of masonry through homogenization theory. Int J Solids Struct 1995;32:137–63.

[3] Bruet BJF, Qi HJ, Boyce MC, Panas R, Tai K, Frick L, et al. Nanoscale morphology and indentation of individual nacre tablets from the gastropod mollusc Trochus niloticus. J Mater Res 2005;20:2400–19.

[4] Barthelat F, Li CM, Comi C, Espinosa HD. Mechanical properties of nacre constituents and their impact on mechanical performance. J Mater Res 2006;21:1977–86.

[5] Cecchi A, Sab K. A multi-parameter homogenization study for modeling elastic masonry. Eur J Mech-A/Solids 2002;21:249–68.

[6] Curnier A, He Q-C, Zysset P. Conewise linear elastic materials. J Elasticity 1995;37:1–38.

[7] Currey JD. Mechanical properties of mother of pearls in tension. Proc Royal Soc Lond 1977;196:443–63.

[8] Currey JD. The mechanical properties of biological materials. In: 34th Symposium of the society for experimental biology. Cambridge University Press; 1980.

[9] Evans AG, Suo Z, Wang RZ, Aksay IA, He MY, Hutchinson JW. Model for the robust mechanical behavior of nacre. J Mater Res 2001;16:2475–84.

[10] Jackson AP, Vincent JFV, Turner RM. The mechanical design of nacre. Proc Royal Soc Lond 1988;234:415–40.

[11] Jäger I, Fratzl P. Mineralized collagen fibrils: a mechanical model with staggered arrangement of mineral particles. Biophys J 2000;79:1737–46.

[12] Ji B, Gao HJ. Mechanical properties of nanostructures of biological material. J Mech Phys Solids 2004;52:1963–90.

[13] Gurtin ME. The linear theory of Elasticity. In: Flügge S, editor. Encyclopedia of physics VIa/2. Berlin: Springer; 1972. p. 1–295.
[14] Katti DR, Katti KS, Sopp JM, Sarikaya M. 3D finite element modelling of mechanical response in nacre-based hybrid nanocomposites. Comp Theo Poly Sci 2001;11:397–404.
[15] Katti DR, Katti KS, Tang J, Pradhan S, Sarikaya M. Modeling mechanical response in a laminated biocomposite. Part II: nonlinear responses and nuances of nanostructures. J Mater Sci 2005;40: 1749–55.
[16] Lin A, Meyers MA. Growth and structure in abalone shell. Mater Sci Eng A 2005;390:27–41.
[17] Menig R, Meyers MH, Meyers MA, Vecchio KS. Quasi-static and dynamic mechanical response of haliotis rufescens (abalone) shells. Acta Mater 2000;48:2383–98.
[18] Nukala PKVV, Simunovic S. Statistical physics models for nacre fracture simulation. Phys Rev E 2005:72. Art. No. 041919.
[19] Pietruszczak S, Niu X. A mathematical description of macroscopic behaviour of brick masonry. Int J Solids Struct 1992;29: 531–46.
[20] Sanchez-Palencia E. Non homogeneous media and vibration theory. Lecture notes in physics, vol. 127. Berlin: Springer-Verlag; 1980.
[21] Sarikaya M. An introduction to biomimetics – a structural viewpoint Microscopy. Res Tech 1994;27:360–75.
[22] Sarikaya M, Gunnison KE, Yasrebi M, Aksay IA. Mechanical properties–microstructural relationship in abalone shell. Mat Res Symp Proc 1990;174:109–16.
[23] Schaffer TE, Ionescu-Zanetti C, Proksch R, Fritz M, Walters DA, Almqvist N, et al. Does Abalone nacre form by heteroepitaxial nucleation or by growth trough mineral bridges? Chem Mater 1997;9:1731–40.
[24] Song F, Soh AK, Bai YL. Structural and mechanical properties of the organic layers of nacre. Biomaterials 2003;24:3623–31.
[25] Timoshenko SP. History of strength of materials. NY: McGraw-Hill Book Company Inc.; 1953.
[26] Wang RZ, Suo Z, Evans AG, Yao N, Aksay IA. Deformation mechanisms in nacre. J Mater Res 2001;16:2485–93.
[27] Willis JR. Mechanics of composites, Unpublished lecture notes, University of Cambridge, 2003.